Experimental Thermal and Fluid Science 109 (2019) 109879

Contents lists available at ScienceDirect

Experimental Thermal and Fluid Science

journal homepage: www.elsevier.com/locate/etfs

An experimental study on dynamic ice accretion process over the surfaces of rotating aero-engine spinners

Linkai Li, Yang Liu, Hui Hu*

Department of Aerospace Engineering, Iowa State University, Ames, IA 50011-2271, United States

ARTICLE INFO

Keywords:
Aero-engine icing physics
Engine spinner design
Rime and glaze icing process
PIV measurements

ABSTRACT

An experimental study was conducted to investigate the dynamic ice accretion process over the surfaces of rotating aero-engine spinners and to examine the detriment effects of the ice accretion on the airflow to be inhaled by aero-engines. Three scaled spinner-fan models with different spinner shapes (i.e., conical-shaped, coniptical-shaped, and elliptical-shaped spinners) were manufactured and exposed under typical *rime* and *glaze* icing conditions for a comparative study. During the experiments, while a high-speed imaging system was used to record the dynamic ice accretion process over the rotating spinner models, a high-resolution particle image velocimetry (PIV) system was utilized to examine the trajectories of super-cooled water droplets as they approach to the surfaces of the spinner models. It was found that, under typical rime conditions, while accreted ice layers were found to conform well with the original shapes of the spinner models in general, the total amount of the ice mass accreted over the spinner surfaces were found to be a strong dependent on the spinner shapes. While the conical-shaped spinner was found to have the largest amount of ice accretion (i.e., 60–80% more than those over the other two spinner models) over almost entire spinner surface, ice accretion was found to take place mainly in the front portion of the coniptical-shaped and elliptical-shaped spinners. Under the glaze icing condition, in addition to forming ice layers over the spinner surfaces, very complicated, needle-shaped icicles were also found to grow rapidly out from the spinner surfaces and extrude into the incoming airflow, due to the effects of the centrifugal forces associated with the rotation motion. The complex glaze ice structures accreted over the spinner surface were found to induce significant disturbances/distortions and even cause large-scale flow separations for the airflow near the iced spinner surfaces, which would significantly degrade the quality of the inlet airflow to be inhaled by aero-engines, thereby, adversely affecting the performance of aero-engines.

1. Introduction

Aero-engine icing, which occurs due to the impinging and subsequent freezing of super-cooled water droplets in clouds on the exposed surfaces of aero-engines, has been widely recognized as a significant hazard to aviation safety in cold weathers. Ice formation/accretion on aero-engine inlet components, such as inlet lip, spinner and fan blades, can significantly degrade the performance of the aero-engines. For example, ice formation/accretion over the rotating spinner and fan blades can result in an imbalanced rotation of the compressor, which would cause serious mechanical vibrations. Furthermore, the shedding of large ice chucks from engine inlet lips, spinners or fan blades may also damage fan rotor and other components behind the fan, or even be sucked into the core of the engine, which can cause severe stall, flameout or surge [1]. While noticeable research progress has been made since 1940s, aero-engine icing remains an important unsolved problem that can threaten aviation safety. More comprehensive studies are highly desirable for a better understanding of the underlying physics pertinent to aero-engine icing phenomena, which would lead to more effective and robust anti-/de-icing strategies to ensure safer and more efficient operation of aero-engines in cold weathers.

As the first engine component to encounter the super-cooled water droplets suspended in the incoming airflow, engine spinner is very susceptible to ice accretion. Upon the impacting of super-cooled water droplets onto the spinner surface, ice layers would be formed and grow into irregular ice structures rapidly over the spinner surface due to the combined effects of the aerodynamic shear forces and the centrifugal force associated with the rotational motion of the spinner. Surprisingly, only a limited number of studies can be found in literature to examine ice accretion on aero-engine spinners. For example, Bidwell et al. [2] investigated ice accretion on the spinner and fan blades of an Energy

* Corresponding author.
E-mail address: huhui@iastate.edu (H. Hu).

https://doi.org/10.1016/j.expthermflusci.2019.109879
Received 1 February 2019; Received in revised form 17 May 2019; Accepted 15 July 2019
Available online 16 July 2019

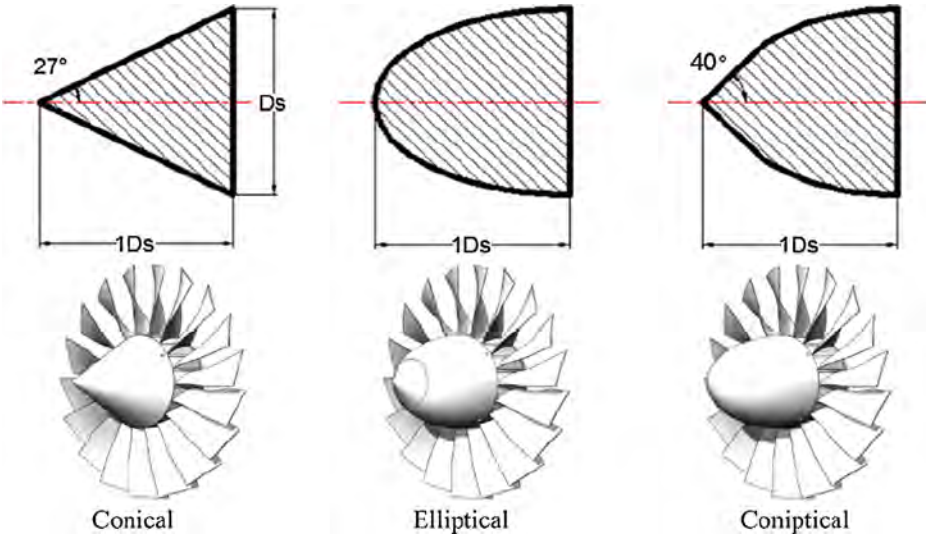

Fig. 1. Schematic of the three sets of spinner-fan models used in the present study.

Efficient Engine (E^3), and reported that water droplets with larger size would result in a faster ice accretion rate over the surfaces of the spinners. Dong et al. [3] conducted a numerical study to investigate ice accretion process on a rotating aero-engine spinner, and found that the temperature of the incoming airflow could significantly affect the icing types and shapes of the ice structures accreted over the spinner surface. Wang et al. [4] investigated the ice accretion and shedding process from a rotating spinner experimentally, and observed a mixture of different types of ice accretion on the spinner surface.

Three different shapes of aero-spinners, i.e., elliptical-shaped, conical-shaped and coniptical-shaped spinners, are widely used in nowadays. As described in Linke-Diesinger [1], while elliptical-shaped spinners were usually found to have a better aerodynamic performance, they were also more easily to get ice accumulated under lower humidity conditions, in comparison to other shaped spinners. On the other hand, conical-shaped spinners were found to have significant ice accretion at relatively higher humidity levels, the aerodynamic efficiency of conical-shaped spinners, however, was found to be lower than that of the elliptical spinners. Hu et al. [5] investigated the effects of the tip angle of a conical-shaped spinner on the ice accretion process, and demonstrated that the tip angle of the conical-shaped spinner would significantly affect the ice accretion over the spinner surfaces. While most of the previous experimental studies were conducted based on acquisition of qualitative ice accretion images, it is highly desirable and essential to conduct quantitative measurements to characterize the dynamic ice accretion process over the surfaces of different shaped spinners in order to gain further insight into the underlying icing physics and to evaluate the resultant detrimental effects induced by the ice accretion over the surface of the spinners.

In the present study, we report a comprehensive experimental investigation to characterize the dynamic ice accretion process on the surfaces of three most-commonly-used engine spinners (i.e., elliptical-shaped, conical-shaped, and coniptical-shaped spinners). The experimental study was performed in an icing research tunnel available at Iowa State University (i.e., ISU-IRT) with scaled aero-engine spinner-fan models exposed into different icing conditions (i.e., *rime* vs. *glaze*). In addition to recording the dynamic ice accretion process over the surfaces of rotating spinner models by using a high-speed imaging system with a "phase-locking" technique, a high-resolution particle image velocimetry (PIV) system was also utilized to quantify the flying trajectories of super-cooled water droplets as they approach to the spinner models. An image processing procedure was developed/implemented to extract quantitative information from the acquired "phase-locked" ice accretion images to characterize the time evolutions of the rime ice layers accreted over the surfaces of different spinner models and to quantify the effects of the spinner shapes on the rime ice thickness/mass accumulated over the surfaces of the three compared spinner models. The characteristics of dynamic ice accretion process over the spinner surfaces were correlated with the trajectories of the super-cooled water droplets in the regions near the spinner surfaces in order to elucidate the underlying physics pertinent to the ice accretion process on the rotating spinner models. The detrimental effects of the ice accretion over the spinner surfaces on the quality of the inlet airflow to be inhaled by engines were also examined based on quantitative PIV measurements. It should be noted that, while a preliminary version of the work was previously reported in a conference paper [6], considerable new results and much more comprehensive discussions/analysis about the measurement results have been added in the present study to gain further insight into the underlying physics of the dynamic ice accretion process over the surfaces of rotating spinner models.

2. Test models and experimental setup

2.1. Test models used in the present study

Three sets of aero-engine spinner-fan models were designed and manufactured for the present study. The spinner-fan models were designed based on the Boeing 18-inch aero-engine test rig as described in Ganz et al. [7]. As shown schematically in Fig. 1, while the fan blades were kept the same for all the three sets of the test models, three most-commonly-used spinners, i.e., elliptical-shaped, conical-shaped and coniptical-shaped spinners, were used for a comparative study. All three spinner models were designed to have the same root diameter (i.e., D_s) and same spinner length. The test models were made of hard-plastic material (i.e., VeroWhitePlus, Stratasys, Inc.) and manufactured by using a rapid prototyping machine (i.e., 3D printer) that builds the test models layer-by-layer with a resolution of about 25 μm. The external surfaces of the test models were further polished with fine sandpapers (i.e., up to 2000 grit) to achieve a very smooth, glossy finish. The primary design parameters of the spinner models used in the present study are summarized in Table 1.

2.2. Icing research tunnel used in the present study

The experimental study was performed in an Icing Research tunnel available at the Department of Aerospace Engineering at Iowa State University (i.e., ISU-IRT). ISU-IRT, which was originally donated by Collins Aerospace System (i.e., formerly Goodrich Corporation), is a

Table 1
Primary design parameters of the aero-engine spinner-fan unit models.

Fan Diameter, D_f (mm)	200	Hub/Tip Ratio	0.402
Spinner Diameter, D_s (mm)	80	Aspect Ratio	1.650
Number of Blades, N	18	Tip Max Thickness/Chord	0.025
Thickness of trailing edge, δ (mm)	0.18	Hub Max Thickness/Chord	0.100

newly refurbished research-grade multifunctional icing research tunnel. It has a test section of 2.0 m in length × 0.4 m in width × 0.4 m in height with all the side walls being optically transparent. ISU-IRT has a capacity of generating a maximum wind speed up to 60 m/s and airflow temperature down to −25 °C. The turbulence level of the oncoming airflow at the entrance of the test section was found to be about 3.0%, as measured by using a hot wire anemometer. Eight pneumatic atomizing spray nozzles are installed (evenly distributed) at the entrance of the contraction section to inject micro-sized water droplets into the airflow. Before performing ice accretion experiments, the characteristics of the water droplet size distribution exhausted from the spray nozzles as a function of the air/water pressure and flowrate supplied to the pneumatic atomizing nozzles were carefully calibrated/evaluated by using a LaVision's ParticleMaster™ imaging system to measure simultaneously size, shape and velocity of the water droplets. With the parameter settings used for the present study, the size of the water droplets in the ISU-IRT was found to range from 10 μm to 100 μm and with the mean volume diameter (MVD) being about 20 μm. By adjusting the water flowrate through the spray nozzles, the liquid water content (LWC) level in ISU-IRT can be adjusted. In summary, ISU-IRT can be operated over a wide range of icing conditions to duplicate/simulate various atmospheric icing phenomena (i.e., from relatively dry *rime* ice to extremely wet *glaze* ice conditions). Further information about ISU-IRT is available at http://www.aere.iastate.edu/icing/ISU-IRT.html.

2.3. Selection of the controlling parameters for the icing experiments

According to the requirements for FAA airworthiness certification, each commercial aircraft or aero-engine with an icing protection system needs to satisfy the strict icing operational requirements as described in FAA Regulation of 14 CFR Part 25 (Airworthiness Standards: Transport Category Airplanes) or Part 33 (Airworthiness Standards: Aircraft Engines) [8–10]. The in-flight icing conditions, which are used to guide ice protection systems design for airframe or aero-engines, are defined in 14 CFR Part 25, Appendix C and Appendix O (Super-cooled Large Drop Icing Conditions). While continuous maximum conditions are usually applied to airframe ice protection, intermittent maximum conditions are commonly referred in the ice protection system design for aero-engines [11]. Therefore, the icing conditions used in the present study were selected based on the intermittent maximum envelope given in the document of FAA 14 CFR Part 25 Appendix C [8].

It is well known that in-flight ice accretion can be either *rime* or *glaze*, depending on the icing conditions [12–14]. When the ambient temperature is relatively low (i.e., typically below −10 °C) and the airflow is relatively dry with a lower liquid water content (*LWC*), supercooled water droplets carried by the airflow would freeze immediately upon impacting onto airframe surfaces, forming *rime* ice. At warmer temperatures, i.e., just below the water freezing temperature, with relatively high *LWC* level in the airflow, the impinged supercooled water droplets would freeze partially, with the remaining water mass transporting along the airframe surface prior to freezing at downstream locations, forming much more complex ice shapes, which is called *glaze* ice. In the present study, while the speed of the incoming airflow was kept in a constant (i.e., V_∞ = 15 m/s) during the icing experiments, both the *rime* and *glaze* ice accretion scenarios over the surfaces of the spinner models were investigated by changing the temperature and *LWC* levels of the incoming airflow in the ISU-IRT. The primary controlling parameters used in the present study to examine the dynamic ice accretion process over the surfaces of the rotating spinner models were listed in Table 2.

In the present study, each trial of the icing experiments was ended after a total amount of 800 g of water mass (i.e., M_{water} = 800 g) was sprayed into ISU-IRT. As shown in Table 2, since the *LWC* level of the incoming airflow for the *rime* icing case (i.e., *LWC* = 1.1 g/m^3) is much lower than that of the *glaze* icing case (i.e., *LWC* = 2.4 g/m^3), the time duration of the rime icing experiments (i.e., total duration of ~308 s) was found to be much longer than that of the glaze icing experiments (i.e., total duration of ~135 s).

It is a common practice to conduct wind tunnel testing with scaled models to predict the performances of prototypes as long as the similitude principles of the wind tunnel testing are satisfied. In the present study, the geometric similarity is satisfied by making the test models having the same geometry shape as the prototype spinners. The kinematic similarity is applied to determine the scaling factor between the flow kinematic parameters around the spinner models used in the present study and those of a typical commercial aero-engine (e.g., CFM56-2/3 engine). More specifically, the kinematic similarity is applied by using the same value of a dimensionless parameter, named as the advance ratio or rotation factor, in order to examine the effects of the rotation motion on the dynamic ice accretion process over the surface of the spinner. As described in Zhang et al. [15], the advance ratio, *J*, is defined as the velocity ratio of the incoming airflow velocity to the moving speed at the fan tip, which is expressed as $J = V_\infty/(\pi \bullet n \bullet D_{fan})$, where V_∞ is the incoming flow speed, *n* is the rotation speed of the spinner-fan model, and D_{fan} is the fan diameter of the test model.

In the present study, a turbofan aero-engine of CFM56-2/3 is used as the design reference to determine the advance ratio for the icing experiments. The CFM56-2/3 aero-engine has an advance ratio of 1.8 (i.e., J = 1.8) at the cruise condition, according to the data sheet released from European Aviation Safety Agency [16]. To match this advance ratio, the rotation speed of the spinner-fan models used in the present study was kept at a constant rotation speed of n = 2500 rpm during the icing experiments, the incoming airflow velocity in test section was set at V_∞ = 15 m/s. Table 3 gives a comparison of the relevant parameters of CFM56-2/3 engine and the test models used in the present study.

2.4. Experimental setup and measurement systems used in the present study

Fig. 2 shows the schematics of the experimental setup used in the present study. An aero-engine spinner-fan model, which was supported by an airfoil-shaped aluminum tube, was placed in the center of the ISU-IRT test section with the rotor disk of the test model being normal to the direction of the incoming airflow. During the experiment, a DC power supply (BK PRECISION 1692) was used to power a brushless

Table 2
Primary controlling parameters used in the icing experiments.

Test Case	Ambient temperature T_∞, (°C)	Airflow speed, V_∞, (m/s)	Liquid Water Content, (g/m^3)	MVD of droplets, (μm)	Model Rotation speed, (rpm)	Test Duration (s)	Icing type
1	−5 °C	15	2.4	20	2500	135	Glaze
2	−10 °C	15	1.1	20	2500	308	Rime

Table 3
A comparison of the relevant parameters of CFM56-2/3 engine and the models used in the present study.

Parameters	CFM 56-2/3	Test models of the present study
Diameter of Fan Rotor (m)	1.52	0.20
Max Rotation Speed (rpm)	5179	3000
Cruising Speed (m/s)	221.0	15.0
Cruising Rotation Speed (rpm)	4900	2500
Temperature Range (°C)	≥ −40	≥ −15
Liquid Water Content (g/m^3)	0.1–3.0	0.1–3.0
Advance Ratio, J	1.80	1.80

motor (Scorpion, SII-4020-420KV) embedded in the aero-engine spinner-fan model. A Proportional-Integral-Derivative (PID) feedback control module along with a data acquisition system (NI, USB-6218) and LabView platform was used to maintain the rotation speed of the spinner-fan model rotating at a constant speed during entire duration of the icing experiment. The rotation speed of the spinner-fan model was monitored by using a digital tachometer (MONARCH PLT200), which can generate a pulsed digital signal from each rotation cycle. The pulsed digital signal was then sent to a Digital Delay Generator (BNC Model-577) to trigger a high-resolution imaging system (PCO. Dimax S4 camera with maximum 2016 pixels × 2016 pixels in resolution) to achieve "phase-locked" image acquisition to reveal the dynamic ice accretion process over the surface of the rotating spinner model. A pair of 200 W Studio-LED lights (RPS Studio Light, Model RS-5620) were used to provide low-flicker illumination in order to ensure high quality of the acquired images.

A high-resolution particle image velocimetry (PIV) system was also used in the present study to characterize the trajectories of super-cooled water droplets as they approach to the spinner model. A double-pulsed Nd:YAG laser (BigSky Corp, EverGreen200@532 nm, 200 mJ/pulse) was used as illumination source for the PIV measurements. A set of optical lenses and mirrors along with a laser delivery arm were used to shape the laser beam into a laser sheet of about 1.0 mm in thickness to illuminate the super-cooled water droplets carried by the incoming airflow. A high-resolution imaging system (PCO. Dimax S4 camera with maximum 2016 pixels × 2016 pixels in resolution) was used for the PIV images acquisition. In order to determine the ensemble-averaged flow quantities, "free-run" PIV measurements were performed by deliberately avoiding the frame rate of the PIV image acquisition being a harmonic frequency of the rotation speed of the spinner-fan model. For the PIV image processing, the interrogation window size was set as 32 pixels × 32 pixels and the effective overlap rate was set as 50%. Under each test section, about 500 frames of instantaneous PIV measurements were used to determine the ensemble-averaged velocity distribution of the super-cooled water droplets around the rotating spinner-fan unit model. The uncertainty level for the instantaneous PIV measurements was estimated to be around 2% and 5% for the ensemble-averaged flow quantities, as described in Tian et al. [17].

3. Measurement results and discussion

In performing the ice accretion experiments, ISU-IRT was operated at a pre-scribed frozen temperature level (e.g., $T_\infty = -10$ °C and −5 °C for the present study) for at least 20 min in order to ensure ISU-IRT reaching a thermal steady state. After the water spray system was switched on, the super-cooled water droplets carried by the incoming airflow would impinge onto the surfaces of the spinner-fan models installed inside ISU-IRT to start ice accretion process. The high-speed imaging system was synchronized with the switch of the water spray system of ISU-IRT in order to reveal the dynamic ice accretion process over the surfaces of the rotating spinner models.

3.1. Acquired "phase-locked" images to reveal the dynamic ice accretion process on the rotating spinner models under a typical rime icing condition

As described above, a "phase-locked" imaging technique was used in the present study to acquire snapshot images of the ice structures accreted on the surfaces of the rotating spinner models as a function of the ice accretion time. Fig. 3 shows some typical "phase-locked" images to reveal the dynamic ice accretion process over the surfaces of the

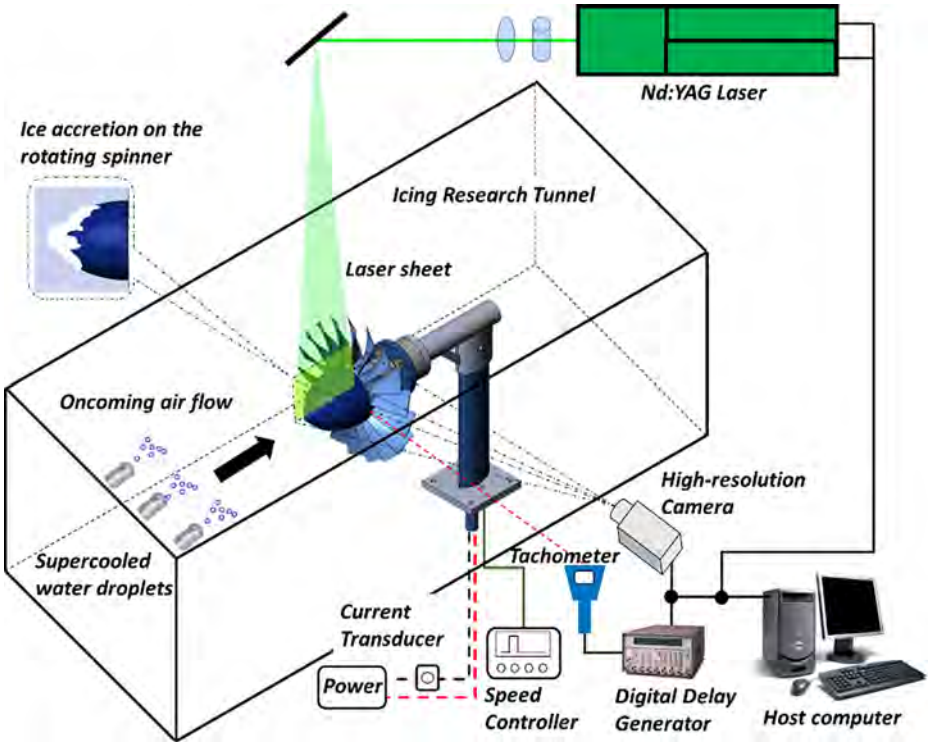

Fig. 2. Experimental setup used in the present study.

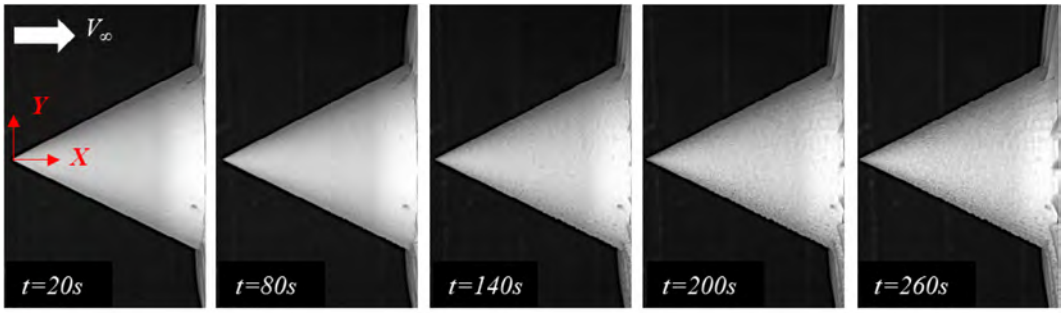

(a). Conical-shaped spinner model

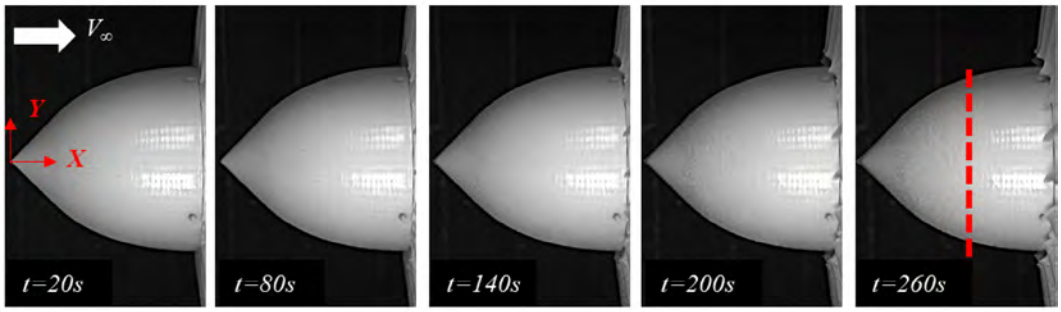

(b). Coniptical-shaped spinner model

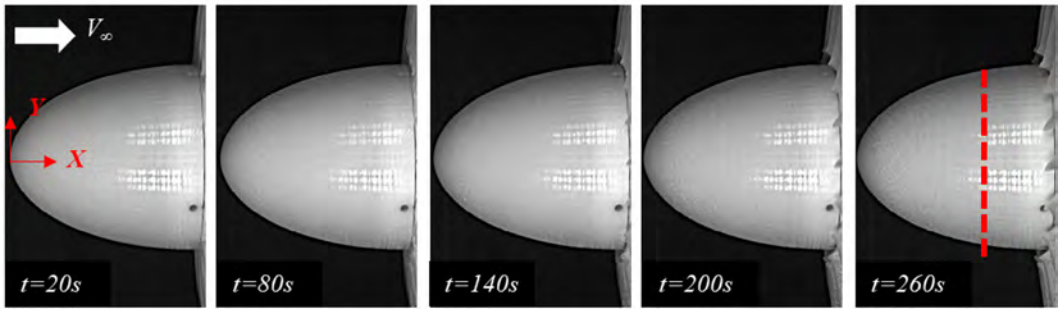

(c). Elliptical-shaped spinner model

Fig. 3. "Phase-locked" images to reveal the dynamic ice accretion process over the surfaces of the rotating spinner models under the typical rime icing condition of $V_\infty = 15$ m/s, $T_\infty = -10$ °C, $LWC = 1.1$ g/m^3, $J = 1.8$.

three compared spinner models under a typical rime icing condition of $V_\infty = 15$ m/s, $T_\infty = -10$ °C, $LWC = 1.1$ g/m^3. It can be seen clearly that, under such a relatively colder and dry test conditions, since the heat transfer process (i.e., both heat conduction via the frozen-cold airflow and heat convection via solid substrate of the test model) would rapidly dissipate the released latent heat of fusion associated with solidification (i.e., phase changing) process, super-cooled water droplets was found to turn into ice instantly upon impacting onto the surfaces of the rotating spinner models. As a result, the ice structures accreted over the surfaces of the spinner models were found to have the characteristics of typical *rime* ice as described in the studies of Liu et al. [14,18], i.e., the accreted ice layers over the spinner surfaces were found to be milk-white in color and opaque in appearance with increased surface roughness. Due to the completely freezing of the super-cooled water droplets upon impacting, no unfrozen water was observed to accumulate over the spinner surfaces, thereby, no surface water runback was found during the rime ice accreting process over the spinner surfaces.

It can also be seen that, while the iced spinner surfaces were found to become relatively rough due to the entrainment of tiny air bubbles between the accreted ice grains, the accreted *rime* ice layers were found to conform well with the original profiles of the spinner models in general. It indicates that, since the super-cooled water droplets would be frozen into ice immediately upon impacting onto the spinner surfaces, the *rime* icing process over the spinner surfaces would almost not be affected by the rotation motion of the spinner models. As the time goes by, with more and more super-cooled water droplets impacting onto the spinner surfaces, the ice layers accreted over the spinner surfaces were found to become thicker and thicker. Although the dynamic rime icing process was found to be quite similar over the surfaces of the three compared spinner models under the rime icing condition, the coverage ranges of ice layers accreted over the spinner surfaces were found to vary greatly, depending on the geometric shapes of the spinners. While *rime* ice accretion was found to take place on almost entire spinner surface for the conical-shaped spinner model, as shown in Fig. 3(a), ice structures were found to accrete mainly in the front portion (i.e., in the range of $X/D_s = 0.0$–0.5) of the spinner surface for the coniptical-shaped spinner model, as revealed in Fig. 3(b). For the test case with the elliptical-shaped spinner model, obvious ice structures were found to accrete mainly in the region of $X/D_s = 0.0$–0.6, as indicated by the red dash line given in Fig. 3(c).

In summary, the acquired ice accretion images given in Fig. 3 reveal clearly that the rime ice layers accreted over the spinner surfaces were found to conform well with the original shape profiles of the spinners in general for all the three compared spinner models. However, the total amount of the ice mass accreted over the spinner surfaces was found to be a strong dependent on the shapes of the spinners, which is deliberated in further details in the next section.

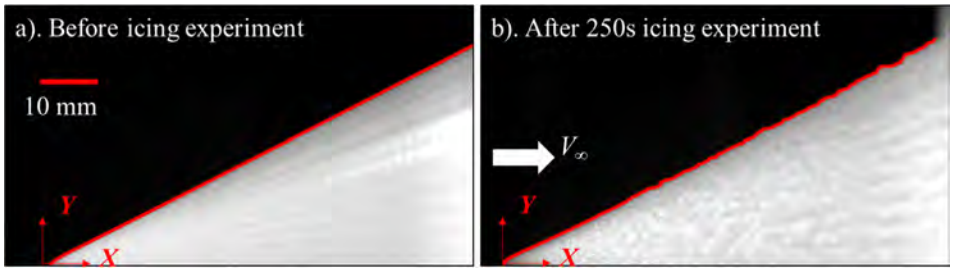

Fig. 4. "Zoom-in" view of the conical-shaped spinner model before and after 250 s of the rime ice accretion.

3.2. Quantification of the rime ice layers accreted over the surfaces of the rotating spinner models

In the present study, an effort was also made to extract quantitative information from the acquired "phase-locked" ice accretion images as those shown in Fig. 3 in order to characterize the *rime* ice layers accreted over the spinner surfaces as a function of the ice accretion time. Fig. 4 shows a "zoom-in" view of the *rime* ice accretion on the conical-shaped spinner model. It can be seen clearly that, in comparison with that of the original surface profile of the spinner (i.e., the profile of the spinner surface before ice accretion as shown in Fig. 4(a)), while the iced spinner surface was found to become much rougher after 250 s of rime icing experiment, the profile of the iced spinner surface would still remain in conical shape in general, as highlighted by the red line in Fig. 4(b). The increased surface roughness due to the rime ice accretion as that shown in Fig. 4(b) would be closely related to the icing conditions (i.e., size of the supercooled water droplets, LWC level, and ambient temperature…). Since the spinner models were exposed under the same rime icing conditions, the characteristics of the increased roughness due to the rime ice accretion over the surfaces of the 3 compared spinner models were found to be very similar.

By using an digital image processing procedure similar as that described in Waldman et al. [19], quantitative information about the characteristics of the rime ice layers accreted over the three compared spinner surface can be extracted from the acquired ice accretion images. The acquired ice accretion images actually represent the maps of the light intensity scattered or reflected from the impinged supercooled water and/or ice structures accreted on airframe surfaces. By deriving the changes of the intensity maps in the time sequences of the acquired ice accretion images, Waldman & Hu [19] developed an image processing algorithm to extract quantitative information to characterize the time evolution of the dynamic ice accretion process over the airfoil surface. With the similar image processing procedure as that described in Waldman & Hu [19], the characteristics of the dynamic rime icing process over the surfaces of the rotating spinner models can be extracted quantitatively from the ice accretion images.

The initial reference image without impacted water or/and ice accretion over the spinner surface, i.e., the image given in Fig. 4(a), was defined as I^0, and the acquired i^{th} image with ice accreted over the spinner surface, e.g., the image given in Fig. 4(b), was defined as I^i. The intensity difference maps for the images of the iced spinner model, thus, can be derived as:

$$I^i_{diff} = I^i - I^0 \tag{1}$$

By conducting such an image processing procedure, the pixel counts in the intensity difference maps would contain the information about the image changes from the initial state (i.e., spinner without water or/and ice) to the iced state with impacted water or/and ice accretion on the spinner. Therefore, the advancing fronts of the ice layers accreted over the spinner surfaces can be identified at every position on the spinner surfaces, x, i.e.,

$$x^i_{ice} = \text{first}(I^i_{diff}(x)^2 > \varepsilon) \tag{2}$$

where ε was chosen as the sixteen standard deviations of the typical image noise as suggested by Waldman & Hu [19]. The image noise was characterized by calculating the root-mean-square (i.e., rms) values of the pixel fluctuations in the blank areas of the images (i.e., areas excluded spinner, ice or water) before ice accretion.

Knowing the initial locations of the spinner leading-edge, i.e., x^i_0, the ice thickness accreted at the leading-edge of the spinner can be calculated as

$$\Delta^i_{ice,img} = K(x^i_{ice} - x^i_0) \tag{3}$$

where K is the calibration constant in mm/pixel.

By applying the image processing procedure described above to the acquired time sequences of the "phase-locked" ice accretion images, the thickness of the rime ice layers accumulated over the surfaces of the rotating spinner models can be extracted quantitatively. Fig. 5 shows the growth of the ice layer accreted over the spinner surfaces as a function of the ice accretion time under the rime icing condition of $V_\infty = 15$ m/s, $T_\infty = -10$ °C and $LWC = 1.1$ g/m^3. It can be seen clearly that, the thickness of the ice layers accreted over the spinner surfaces would increase continuously as the ice accretion time increases, as expected. The thickness of the accreted ice layer was found to be rather uniform on the conical-shaped spinner (i.e., the ice thickness was found to be almost the same value from the spinner nose to the root) as shown in Fig. 5(a). However, the rime ice layers accreted on the coniptical-shaped and elliptical-shaped spinners were found to be vary greatly from the nose to the spinner root, with the ice thickness being the maximum at the spinner nose and decreasing gradually at further downstream locations, as shown clearly in Figs. 5(b) and 6(c). The thickness of the ice layer was found to become almost zero (i.e., $\Delta_{ice} \approx 0.0$) at the downstream location of $X/D_s \approx 0.60$ for the coniptical-shaped spinner model, and at the downstream location of $X/D_s \approx 0.65$ for the elliptical-shaped spinner model. The thickness variations of the ice layers on different spinner models were believed to be closely related to the distinct differences in the impingement characteristics of the supercooled water droplets onto the surfaces of the three compared spinner models, which will be investigated further in next section of the present study.

Based on the measured thickness distributions of the ice layers over the spinner surface as those shown in Fig. 5, the growth rates of the accreted ice layers over the spinner surfaces as a function of the ice accretion time can also be determined. Fig. 6 shows the time evolution of the measured thickness of the ice layers at three selected locations over the surfaces of the three compared spinner models. While the thickness of the accreted ice layers over the spinner surfaces were found to increase almost linearly with the ice accretion time, the increasing rates of the ice layers were found to vary greatly, depending on the shapes of spinner models. For the conical-shaped spinner model, as shown in Fig. 6(a), the ice layer accreted near the sharp spinner nose was found to increase very rapidly with the maximum growth rate of 0.0147 mm/s (i.e., $d\Delta/dt \approx 0.0147$ mm/s). The growth rate of the ice layer at other downstream locations was found to be much more moderate, having almost the growth rate value and resulting in a rather uniform ice layer accreted over the surface of the conical-shaped

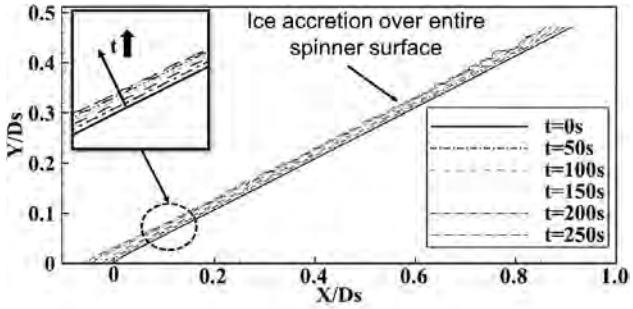

(a). Conical-shaped spinner model

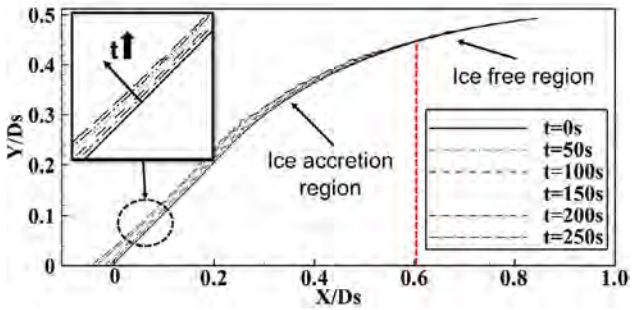

(b). Coniptical-shaped spinner model

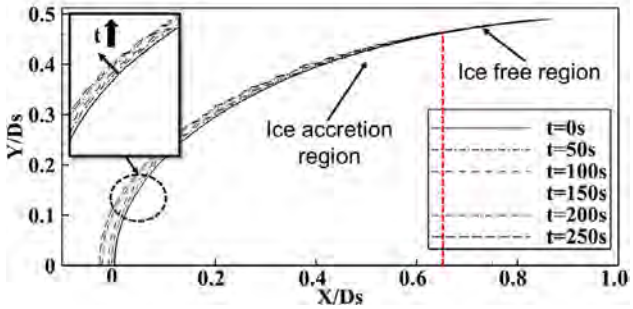

(c). Elliptical-shaped spinner model

Fig. 5. The profiles of the ice layers accreted over the surfaces of the three compared spinner models under the rime icing condition.

spinner model, as shown in Fig. 6(a).

For the coniptical-shaped spinner model, as shown in Fig. 6(b), while the thickness of the ice layer accreted near the spinner nose was found to have the largest growth rate of 0.0123 mm/s (i.e., $d\Delta/dt \approx 0.0123$ mm/s), the growth rate of the ice layer was found to decrease rapidly as the downstream distance from the spinner nose increases (i.e., $d\Delta/dt \approx 0.0056$ mm/s at the downstream location of $X/D_s = 0.25$, and $d\Delta/dt \approx 0.0032$ mm/s at $X/D_s = 0.50$). For the test case with the elliptical-shaped spinner model, while the growth rate of the ice thickness at the spinner tip was found to be about 0.009 mm/s (i.e., $d\Delta/dt \approx 0.0090$ mm/s), the growth rates of the accreted ice layer were found to become much smaller at the downstream locations, i.e., $d\Delta/dt \approx 0.0064$ mm/s at the downstream location of $X/D_s = 0.25$, and $d\Delta/dt \approx 0.0020$ mm/s at $X/D_s = 0.50$, as shown in Fig. 6(c).

Based on the measured ice thickness data as those shown in Fig. 5, total ice mass accreted over the spinner surfaces as a function of the ice accretion time can also be determined with the following equation.

$$M_{rime} = \rho_{rime} \int_{r=0}^{r=0.5D_s} \Delta(r) \cdot 2\pi r \cdot dr \tag{4}$$

where ρ_{rime} is the *rime* ice density as given in Vargas et al. [20] and Liu et al. [14] (i.e., $\rho_{rime} \approx 0.88$ g/cm^3); $\Delta(r)$ is the thickness of the rime layer accreted over the surfaces of the spinner models with the radius of r.

Fig. 7 shows the time evolution of the total ice mass accreted on the three compared spinner models. It can be seen clearly that, the time dependences of the total ice mass accreted over the spinner surfaces were found to be fit well with linear functions for all three spinner models. With the spinner model exposed under the same rime icing condition of $V_\infty = 15$ m/s, $T_\infty = -10$ °C, $LWC = 1.1$ g/m^3 and $J = 1.8$, the total ice mass accreted on the surface of the conical-shaped spinner model was found to increases much faster than the other two cases. After about 250 s of rime icing experiment, the total ice mass accreted on the conical-shaped spinner model was found to be about 11.8 g, which is about 160–180% of the total ice mass accreted on the other two spinner models (i.e., the corresponding values were 6.6 g and 7.2 g on the surfaces of the coniptical-shaped and elliptical-shaped spinner models, respectively).

It should be noted that, based on the ice accretion images similar to those shown in Fig. 3, Linke-Diesinger [1] suggested that elliptical-shaped spinners would be more easily to have ice accumulation under lower humidity conditions (i.e., rime icing condition), in comparison to other shaped spinners. Such a conjecture was based on the experimental observation of thicker ice layer accreted near the nose of the elliptical-shaped spinner, as shown in Fig. 5(c). The quantitative measurements of the present study reveal clearly that, the conical-shaped spinner model is actually most susceptible to ice accretion (i.e., having 60–80% more in accreted ice mass) with the accreted ice layer covering the entire spinner surface. The coniptical-shaped and elliptical-shaped spinner models were found to have very similar ice accretion characteristics under the rime icing condition.

3.3. PIV measurements to quantify the trajectories of super-cooled water droplets near the spinner models

As described above, a high-resolution PIV system was used in the present study to quantify the trajectories of the super-cooled water droplets in the regions around the spinner models in order to gain further insight into the underlying physics associated with the ice accretion process over the surfaces of the spinner models. During the experiment, the super-cooled water droplets carried by the incoming airflow were used as the tracers for the PIV measurements. Fig. 8 shows the time-averaged PIV measurement results in the term of the streamlines of the supper-cooled water droplets around the three compared spinner models under the rime icing condition of $V_\infty = 15$ m/s, $LWC = 1.1$ g/m^3, $T_\infty = -15$ °C and $J = 1.8$. As shown in Fig. 8(a), the streamlines near the conical-shaped spinner model were found to deviate only slightly along the spinner surface as the super-cooled water droplets approach to the spinner surface. Due to the effects of the inertia forces, the super-cooled water droplets would be more likely to remain in their initial moving direction, thereby, would impinge onto almost the entire surface of the spinner model. It indicates that the impinging zone of the supercooled water droplets would cover entire surface of the conical-shaped spinner model, i.e., from the nose ($X/D_S = 0.0$) to the root (i.e., $X/D_S = 1.0$), as indicated clearly in the sketch given in Fig. 8(a).

As revealed from the PIV measurement results given in Fig. 8(b) and (c), however, as the super-cooled water droplets approach to the surfaces of the coniptical-shaped and elliptical-shaped spinner models, the trajectories of the super-cooled water droplets were found to change significantly, especially near the surface at the front portions of the spinner models, due to the dramatic changes in the geometric shape profiles of the spinner models. Consequently, the super-cooled water droplets would be more likely to impact onto the front surfaces (i.e., mainly in the region of $X/Ds = 0.0$–0.50) of the spinner models. Therefore, the impinging zone of the super-cooled water droplets would concentrate mainly at the front half spinner surfaces for the coniptical-shaped and elliptical-shaped spinner models, as shown schematically in Fig. 8.

Based on the PIV measurement results, a critical streamline can be identified for each test cases, which is also shown as the red dashed

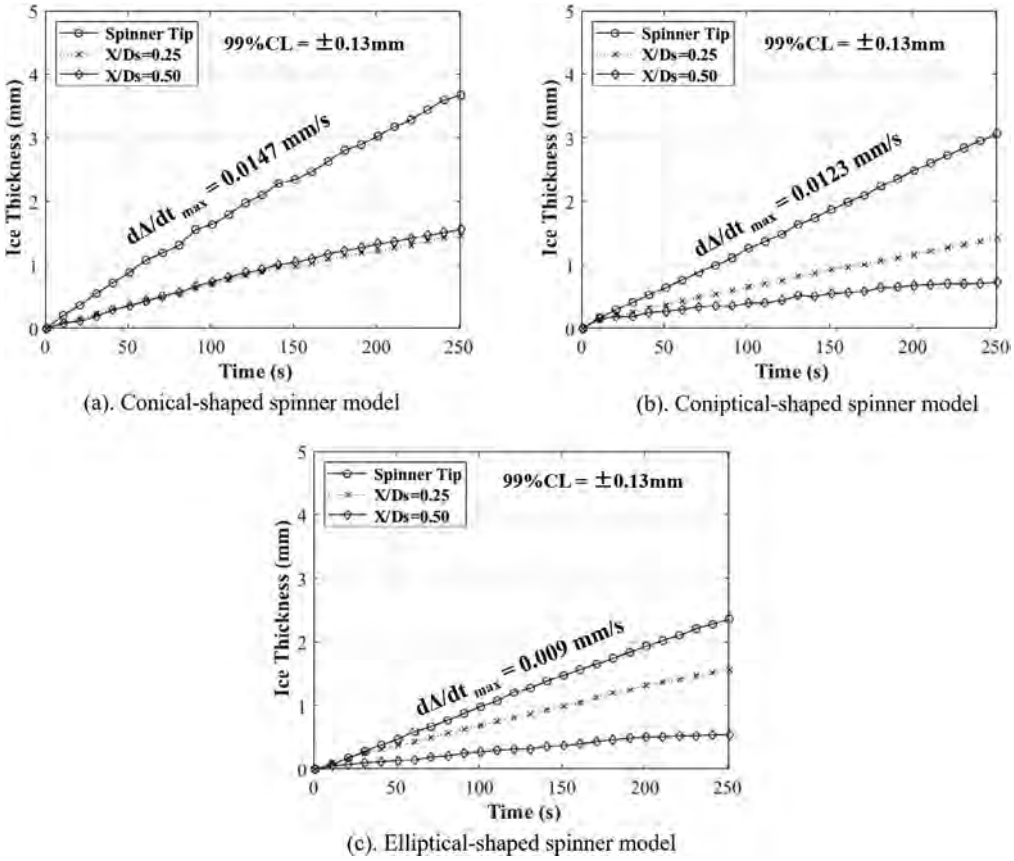

Fig. 6. The time evolution of the ice layer thickness at different selected locations over the surface of the spinner models under the rime icing condition.

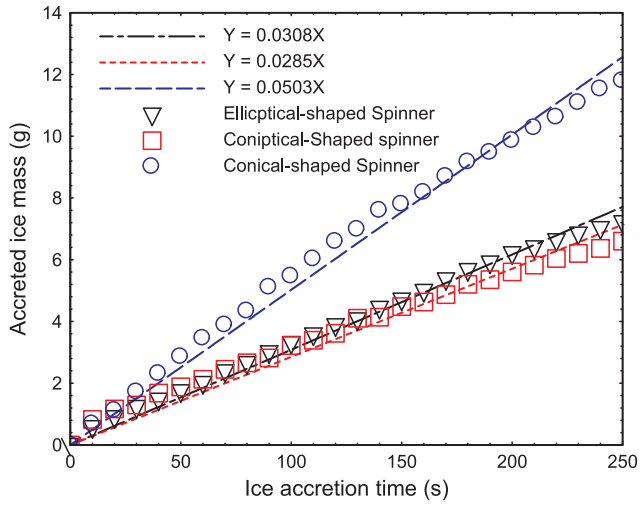

Fig. 7. Time evolution of the total ice mass accreted over the surfaces of the three compared spinner models under the rime icing test condition.

lines in Fig. 8. With the supercooled water droplets approaching the spinner model at the locations above the critical streamlines, they would not be able to impinge onto the surfaces of the tested spinner models. The intersecting point of the critical streamline with the spinner surface would define the impingement limit of the supercooled water droplets, i.e., the farthest downstream location of the impinging zone of the supercooled water droplets. Since supercooled water droplets would be frozen into ice instantly upon impinging onto the spinner surfaces under the rime icing conditions, the impingement limit of the supercooled water droplets on the spinner surface would also indicate the coverage of the rime ice layer accreted over the spinner surface.

As described above, since the impinging zone of the supercooled water droplets would cover entire spinner surface for the conical-shaped spinner model, rime ice accretion was found to take place over the entire spinner surface, as shown quantitatively in Fig. 5(a). As shown in the PIV measurement results given in Fig. 8, the impingement limits of the supercooled water droplets were found to be located of X/Ds ≈ 0.60 and X/Ds ≈ 0.65 on the surfaces of the coniptical-shaped and elliptical-shaped spinner models, respectively. The impingement limits revealed from the PIV measurements were found to coordinate well with the coverage ranges of the rime ice layers over the surfaces of the coniptical-shaped and elliptical-shaped spinner models identified from acquired "phase-locked" ice accretion images, as shown in Fig. 5.

3.4. Dynamic ice accretion process over the surfaces of rotating spinner models under a glaze icing condition

With the rotation speed of the spinner models and the airflow velocity in ISU-IRT being kept at the same values (i.e., n = 2500 rpm; and V_∞ = 15 m/s) as those used for the rime icing experiments, an experimental study was also performed to examine the dynamic glaze ice accreting process over the surfaces of the rotating spinner models under a typical glaze icing condition, i.e., with a warmer temperature of $T_\infty = -5$ °C and a higher *LWC* level of *LWC* = 2.4 g/m^3. Fig. 9 gives some of the acquired "phase-locked" images, which reveal the characteristics of the dynamic glaze icing process over the surfaces of the rotating spinner models clearly.

In comparison to the rime icing scenario described above, due to the higher LWC level in the incoming airflow under the glaze icing condition, much more supercooled water droplets would impact onto the surfaces of the spinner models within the same duration of the icing experiments. Corresponding to the solidification of much larger

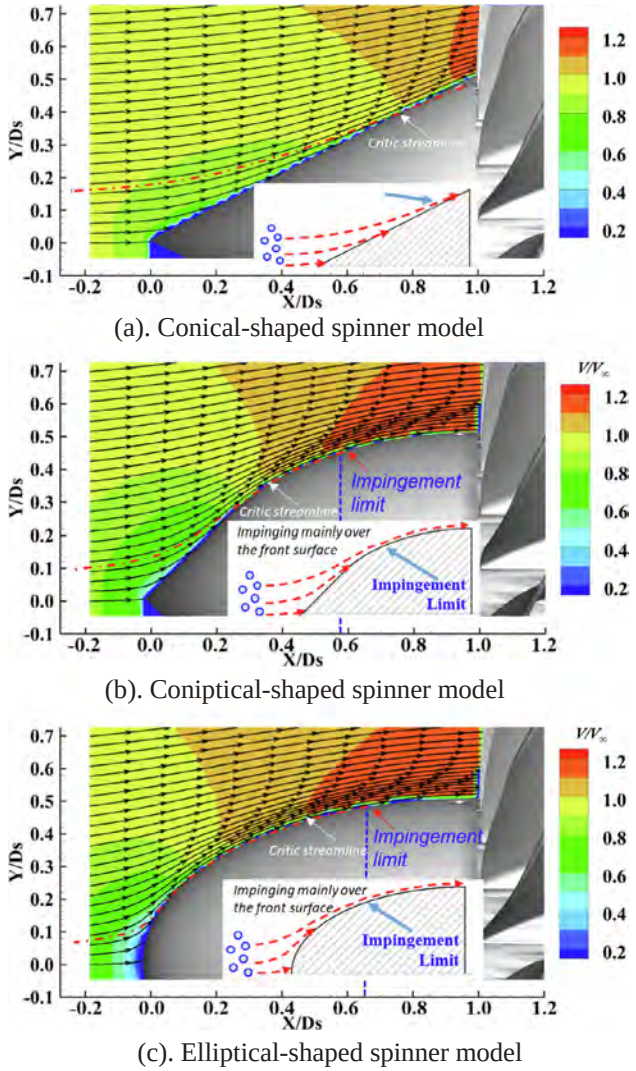

Fig. 8. PIV measurements to reveal the trajectories of the super-cooled water droplet around the spinner models.

amounts of the impinged water mass, much greater amount of the latent heat of fusion would be released over the spinner surfaces within the same duration of the time under the glaze icing condition. However, as described in Liu & Hu [21], due to the much warmer ambient temperature (i.e., $T_\infty = -5\,^\circ C$) under the glaze icing condition, the heat transfer process could not dissipate all the released latent heat of fusion instantly. As a result, while only a portion of the supercooled water droplets would be frozen into solid ice upon impacting on to the spinner surfaces, the rest of the impacted water mass would still stay in liquid phase, which can flow freely over the ice accreting spinner surfaces. Due to the combined effects of the aerodynamic shear forces exerted by the airflow and the centrifugal force inducted by the rotation motion of the spinner models, the glaze ice accretion process over the surfaces of the rotating spinner models were found to become much more complicated, in comparison to the rime ice accretion scenario described above.

As revealed clearly from the acquired ice accretion images given in Fig. 9, the dynamic glaze ice accretion process over the surfaces of the rotating spinner models was found to be affected by the geometric shapes of the spinners significantly. Since the impingement zone of the supercooled water droplets would cover entire surface for the conical-shaped spinner model as revealed by the PIV measurements described above, the impinged water droplets were found to coalesce first to a form water film/ice layer rapidly to cover almost entire surface of the conical-shaped spinner model at first, as shown in Fig. 9(a). As the ice accretion time increases, with more and more supercooled water droplets impacting onto the spinner surface, the unfrozen water mass accumulated over the spinner surface was found to increase dramatically. As driven by the aerodynamic shear force exerted by the incoming airflow, the unfrozen surface water was found to run back from the spinner nose to the spinner root quickly. Meanwhile, due to the effects of the centrifugal force associated with the rotation motion, a portion of the runback water was found to take off from the ice accreting surface of the spinner model, and was then frozen subsequently to form very complicated, needle-liked icicles extruding outward into the airflow, as shown clearly in snapshot images acquired at the time of $t \geq 75$ s. It can also be seen that the formation of the needle-liked icicle structures was found to be more significant at the further downstream locations near the spinner root due to the stronger centrifugal forces associated with the larger diameters near the spinner root. After about 120 s of the ice accretion experiment (i.e., $t \geq 120$ s), the needle-liked icicle structures were found to be formed over most of the spinner surface (i.e., in the range of $X/D_s \approx 0.25$ to $X/D_s = 1.0$), as shown clearly in the "phase-locked" ice accretion image acquired at the time of $t = 135$ s.

Fig. 9(b) shows a set of the acquired "phase-locked" ice accretion images over the surface of the rotating coniptical-shaped spinner model. It can be seen clearly that, at the time instant of $t = 15$ s and $t = 45$ s, a layer of water/ice mixtures was found to be formed quickly over the spinner surface in the region near the spinner nose, due to the direct impingement of the super-cooled water droplets carried by the incoming airflow as revealed from the PIV measurement result given in Fig. 8(b). Unlike that over the surface of the conical-shaped spinner model, ice accretion over the surface of the coniptical-shaped spinner model was found to concentrate mainly at the front portion of the spinner (i.e., in the range from $X/D_s = 0.2$–0.65), while the rear part of the spinner surface was found to be almost free of water/ice. As ice accretion time increases by, more and more supercooled water droplets would impinge onto the spinner surface. Due to the combined effects of the aerodynamic shear force exert by the incoming airflow and the strong centrifugal force associated with the rotation motion, very complex, needle-liked icicles were also found to grow rapidly outward from the front surface of the spinner model, as revealed in the snapshot images acquired at the time instants of $t = 75$ s and $t = 135$ s. Since the centrifugal force acting on the impacted water mass in the region near the spinner nose would be very small due to the small diameter near the spinner nose, no needle-liked icicles were found to form in the region near the spinner nose (i.e., in the region of $X/Ds < 0.2$). It can also be observed that, since the direct impinging zone of the supercooled water droplets was found to be mainly at the front surface of the coniptical-shaped spinner model (i.e., the impinging limit was found to be at $X/D_s \approx 0.60$ as shown in Fig. 9(b)), and the much stronger centrifugal force acting on the runback surface water on the rear spinner surface would make the runback water to take off from the spinner surface before reaching to the downstream locations near the spinner root, thus, the rear portion of the coniptical-shaped spinner model (i.e., in the region of $X/Ds > 0.70$) was found to be totally ice free during the entire ice accretion experiment. It can also be seen clearly that, while the formation of the needle-liked icicle structures was found to be much closer to the root nose, the coverage of the complicated icicle structures was found to be much less on the coniptical-shaped spinner model, in comparison with that on the conical-shaped spinner model.

For the elliptical-shaped spinner model, as shown clearly in Fig. 9(c), while the formation of the needle-liked icicle structures over the spinner surface was found to take place much earlier in time and much more closer to the spinner nose (i.e., starting from downstream location of $X/D_s \approx 0.10$), the area covered with the needle-liked icicle structures on the spinner surface was found to be much smaller for the elliptical-shaped spinner model, in comparison with the other two compared spinner models. As a result, most of spinner surface at the rear portion of the elliptical-shaped spinner model (i.e., beyond the

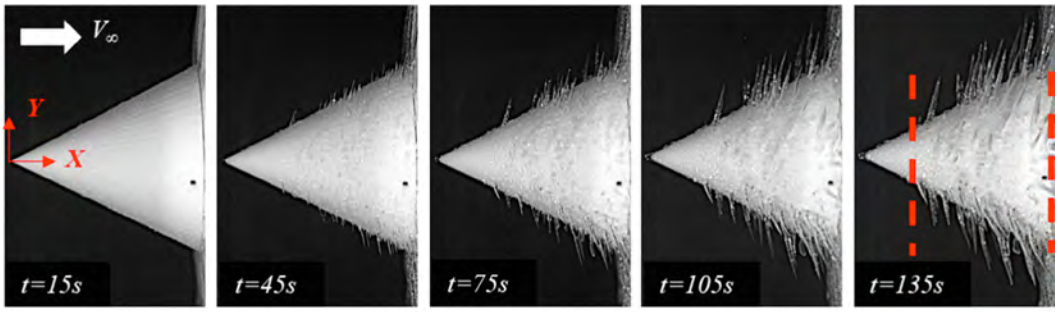

(a). Conical-shaped spinner model

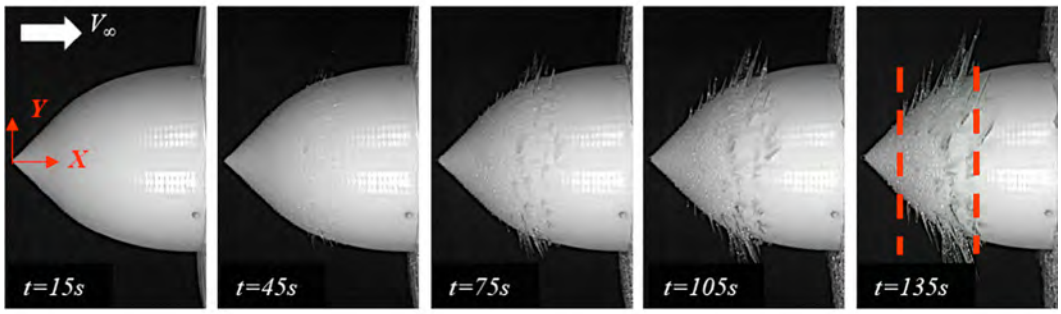

(b). Coniptical-shaped spinner model

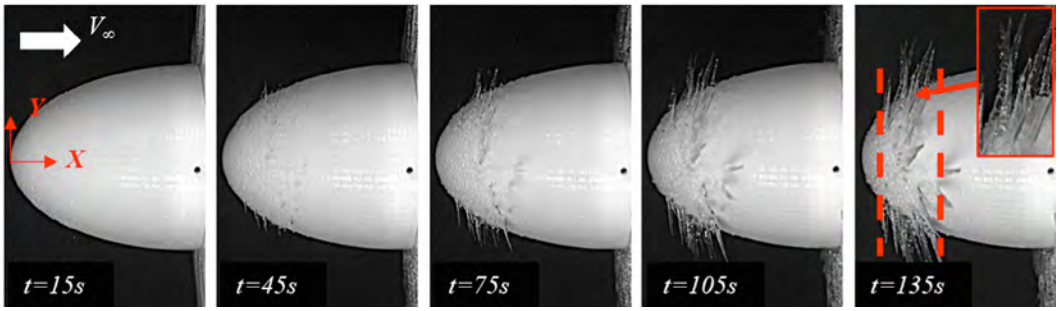

(a). Elliptical-shaped spinner model

Fig. 9. Snapshot images to reveal the dynamic ice accretion process over the surfaces of the three spinner models under the typical glaze icing condition of $V_\infty = 15$ m/s, $T_\infty = -5$ °C, $LWC = 2.4$ g/m^3, and $J = 1.8$.

downstream region of X/D$_s$ ≈ 0.50) was found to be completely free of ice during the entire glaze icing experiment.

The significant differences in the glaze ice accretion on the surfaces of the three compared spinner models are believed to be closely related to the variation characteristics of the centrifugal forces acting on the runback water on the spinner surfaces. In the present study, normalized centrifugal force acting on the runback water on the surface of a rotating spinner model is defined as:

$$C_{Fc} = \frac{F_{c,r}}{F_{c,r=\max}} = \frac{m\omega^2 r}{m\omega^2 r_{\max}} = \frac{r}{r_{\max}} \quad (5)$$

where m is the mass of the runback water, ω is the angular rotation speed of the spinner model, r is the radius of the location of the runback water on the spinner surface, and r_{max} is the maximum radius at the bottom of the spinner model (i.e., at X/Ds = 1.0).

Fig. 10 shows the profiles of the normalized centrifugal forces acting on the runback water as a function of the downstream location over the surfaces of the rotating spinner models. It can be seen clearly that, the variations centrifugal forces acting on the runback water over the spinner surfaces are highly dependent on the geometric shapes of the spinners. The magnitude of the centrifugal force acting on the runback water on the surface of the elliptical-shaped spinner model was found to be much higher than those over the surfaces of the other two spinner

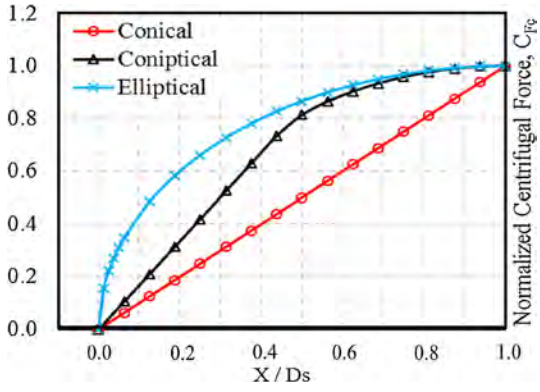

Fig. 10. Variations of the centrifugal forces acting on runback water over the surfaces of the rotating spinner models.

models, especially in the region near the spinner nose (i.e., $X/Ds = 0.0$ to $X/Ds = 0.30$). Due to the much stronger centrifugal force acting on the runback water, instead of flowing downstream along the spinner surface, the runback water would be much more likely to take off from the spinner surface to form needle-liked icicles over the front surface of

the elliptical-shaped spinner model, as shown clearly in Fig. 9. On the other hand, since the centrifugal force acting on the runback water would be much smaller over the front portion of the spinner surface for the conical-shaped spinner model, the impacted water on the surface of the conical-shaped spinner model would be able to stay on the spinner surface, running back along the spinner surface to reach further downstream locations as driven by the aerodynamic shear force exerted by the incoming airflow. As shown in Fig. 10, the centrifugal force acting on the runback water over the conical-shaped spinner model would increase linearly with the local radius on the spinner surface. Due to the stronger centrifugal forces acting on the runback water at the further downstream locations, the runback water was found to take off from the surface of the conical-shaped spinner model to form needle-liked icicle structures subsequently, as clearly shown in Fig. 9(a).

While the variation characteristics of the centrifugal force acting on the runback water over the surface of the coniptical-shaped spinner model were found to be very similar as those of the conical-shaped spinner model at the front portion of the spinner surface (i.e., increase linearly with the local radius on the spinner surface), they become very similar as those of the elliptical-shaped spinner model on the rear portion of the spinner surface (i.e., centrifugal force becoming much greater to make runback water take off from the spinner surface). As a result, the accreted glaze ice structures (i.e., forming complicated needle-liked icicles) over the surface of the coniptical-shaped spinner model (i.e., in the region of X/Ds $<$ 0.5) were found to be quite similar as those on the conical-shaped spinner model at the front portion of the spinner surface. Due to the much greater centrifugal force values over the rear portion of the spinner surface, no runback surface water/accreted ice structures would be able to stay on the surface of the rotating coniptical-shaped spinner model. Therefore, the rear portion of the coniptical-shaped spinner surface was found to be totally ice free, as shown in Fig. 9(b). In summary, the variation characteristics of the centrifugal force acting on the runback water over the spinner surfaces can be used to explain the experimental observations, e.g., why the needle-liked icicle structures were found to form mainly at the front portion of the elliptical-shaped spinner model, but were found to be at much further downstream locations on the conical-shaped spinner model. Among the three compared spinner models, the conical-shaped spinner model was found to be the most susceptible to generate needle-liked icicle structures over the rotating spinner surface under the glaze icing condition, which confirms the conjecture described in Linke-Diesinger [1].

3.5. PIV measurements to reveal the detrimental effects of the ice accretion over the spinner surfaces on the quality of the inlet airflow

It is well known that ice formation/accretion on aero-engine inlet components, such as inlet lip, spinner and fan blades, can significantly degrade the performance of the aero-engine. The ice formation/accretion over the rotating spinner and fan blades can result in an imbalanced rotation of the compressor, which would cause serious mechanical vibrations. Furthermore, shedding of large ice chucks from engine inlet lips, spinners or fan blades may also damage the fan rotor and the components behind the fan, or even be sucked into the core of the engine, which can cause severe stall, flameout or surge [22,23]. It should also be noted that, the ice formation/accretion on aero-engine inlet components such as on the spinner surface would also degrade the quality of the inlet airflow to be inhaled by the aero-engines (e.g., increase turbulence intensity levels and even cause flow separations), thereby, adversely affecting the performance of the aero-engine.

In the present study, the high-resolution digital PIV system was also used to quantify the airflow fields around the three compared spinner models before and after ice formation/accretion over the spinner surfaces in order to reveal the significant changes of the airflow fields around the spinner models induced by of the ice accretion over the spinner surfaces. The PIV measurement plane was selected to pass the symmetrical plane of the axisymmetric spinner models. The PIV measurements were performed under a “free-run” mode (i.e., the rate of the PIV image acquisition was pre-selected at a frequency that is not a harmonic frequency of the rotating frequency of the spinner model, similar as the technique used by Tian et al. [17]) in order to ensure physically meaningful measurements of the ensemble-averaged airflow quantities.

To conduct the PIV measurements to quantify the airflow fields around the rotating spinner models for the test case before having ice formation/accretion over the spinner surfaces (i.e., before switching on the water spray system of ISU-IRT), a smoke generator was used to generate ~1 μm oil droplets to seed the incoming airflow in the test section of ISU-IRT. The PIV measurement results with the “clean spinner models” (i.e., without ice formation/accretion over the spinner surfaces) were used as the comparison baselines to reveal the significant changes in the airflow fields around the spinner models induced by ice accretion. After switching on the water spray system, the super-cooled water droplets suspended in the incoming airflow would impact onto the spinner models to start the dynamic ice accretion process. As the ice accretion time increases, ice structures accreted over the surfaces of the spinner models would grow up rapidly, resulting in much roughed spinner surfaces under the dry rime icing condition as shown in Fig. 3 or formation of very complicated needle-liked icicles over the spinner surfaces under the wet glaze icing conditions as shown in Fig. 9. After reaching a pre-scribed ice accretion time (e.g., 90 s after glaze icing experiment as shown in Fig. 11), the water spray system of ISU-IRT was turned off, but the smoke generator was turn on to generate ~1 μm oil droplets as the PIV tracers to seed the incoming frozen-cold airflow. Then, PIV measurements were performed to quantify the airflow fields around the iced spinner models.

In the present study, 500 frames of instantaneous PIV measurements obtained under “free-run” mode were used to determine the ensemble-averaged velocity fields of the airflow around the rotating spinner model for each test cases. As shown clearly in the acquired ice accretion images given in Fig. 3, the rime ice layers accreted over the surfaces of the spinner models were found to conform well with the original shapes of the spinner models in general for all the three studied spinner models. As a result, the effects of the rime ice accretion over the spinner models on the airflow fields around the spinner models were found to be relatively weak, as expected. Therefore, the PIV measurement results for the test cases with rime ice accretion over the surfaces of the spinner models are not presented here for conciseness. However, under the glaze icing condition, very complicated, needle-shaped icicles were also found to grow rapidly out from the spinner surfaces and extrude into the incoming airflow, due to the effects of the centrifugal forces associated with the rotation motion. The complex glaze ice structures accreted over the spinner surface were found to induce significant disturbances/distortions to the airflow near the iced spinner surfaces.

Fig. 11 shows the typical pictures of the ice structures accreted over the spinner surfaces after 90 s of the glaze icing experiment with $V_\infty = 15$ m/s, $LWC = 2.4$ g/m^3, $T_\infty = -5$ °C and $J = 1.8$, along with the corresponding PIV measurement results. It should be noted that, in order to highlight the detrimental effects induced by the ice accretion over the spinner surfaces on the quality of the inlet airflow to be inhaled by aero-engines, the differences in the measured velocity vectors between the test cases with iced spinner models (i.e., PIV measurements after 90 s of glaze icing experiment) and the corresponding baseline cases with “clean spinner models”, i.e., $\Delta\vec{V} = \vec{V}_{iced} - \vec{V}_{clean}$, are plotted in the figures for the comparison.

It can be seen clearly that, even only after 90 s of the glaze icing accretion experiment, the ice structures accreted over the spinner surfaces were found to cause significant changes/disturbances to the airflow fields around the spinner surfaces. More specifically, ice structures accreted over the spinner surfaces were found to cause obvious reductions in the airflow speed in the regions near the iced spinner

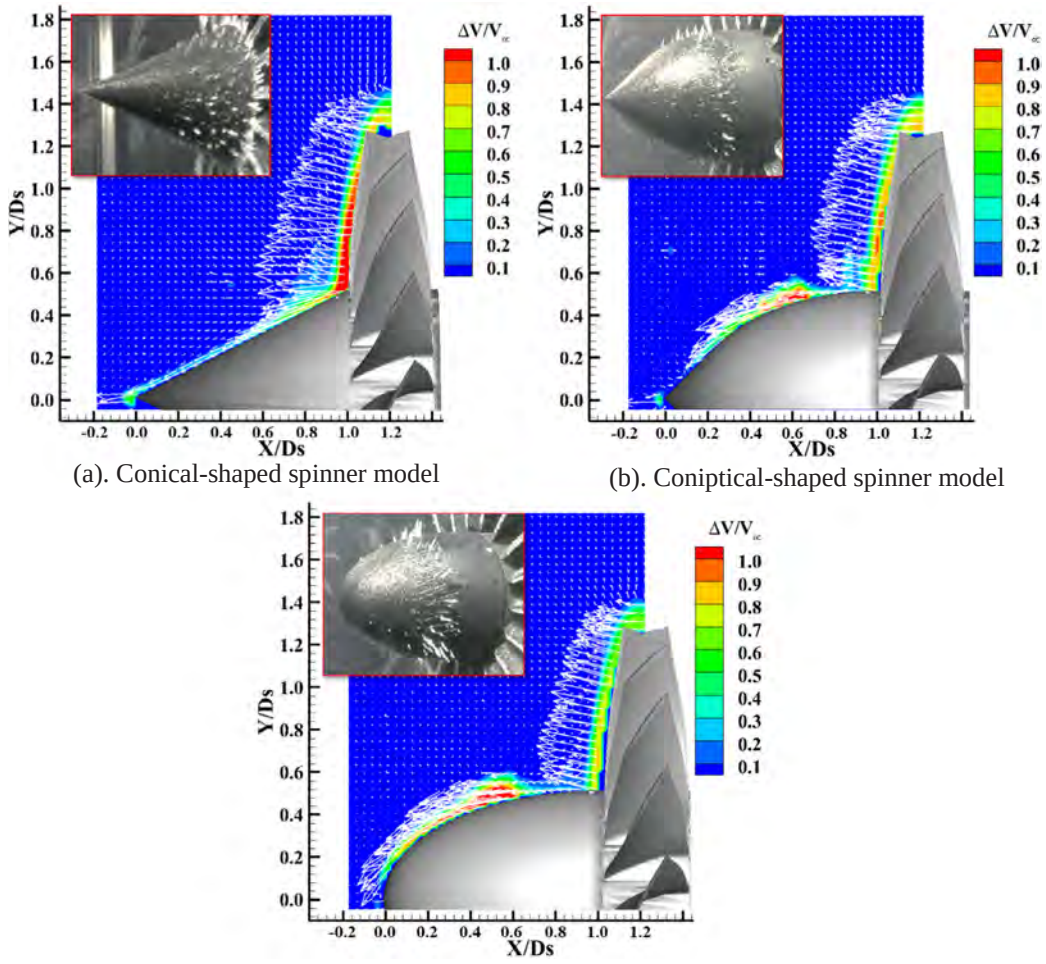

Fig. 11. PIV measurements to reveal the significant changes of the flow fields around the spinner models after 90 s of the glaze icing experiment with $V_\infty = 15$ m/s, $T_\infty = -5$ °C, $LWC = 2.4$ g/m^3, $J = 1.8$.

surfaces (e.g., as indicated by the significant reversing velocity vectors), and induce large-scale flow separations behind the needle-liked icicles accreted over the spinner surfaces. Such disturbances would significantly degrade the quality of the inlet airflow to be inhaled by the aero-engines (i.e., causing non-uniformity in the inlet airflow and increasing turbulence intensity levels). As shown clearly in Fig. 11, the detrimental effects induced by the ice accretion were found to be more obvious for the airflow field around the elliptical-shaped spinner model (i.e., much greater flow separation regions over the spinner surface) in comparison to the other two spinner models. This is believed to be closely related to the much earlier formation of the complicated needle-liked icicles near the nose of the elliptical-shaped spinner model, as shown in Fig. 9. Among the three compared spinner models, since the s needle-liked icicles were found to be generated at much later in time and at further downstream locations on the conical-shaped spinner model, the detrimental effects induced by the ice accretion seems to be much less for the airflow around the conical-shaped spinner model.

It can also be seen that, the ice structures accumulation along the leading edges the rotating fan blades were also found to cause significant "block effects" to the incoming airflow, which would significantly decrease the total amount of the inlet airflow to be inhaled by the aero-engine. As the ice accretion time increases, with more and more supercooled water droplets impacting onto the surfaces of the spinner and fan blades, the ice structures accreted on the surfaces of the rotating spinner and the fan blades would grow bigger and bigger, which would result in more severe detrimental effects to the inlet airflow to be inhaled by the aero-engine. In summary, as revealed from the PIV measurement results given in Fig. 11, the ice formation/accretion on the aero-engine inlet components, such as on the surfaces of the rotating spinner and fan blades, could significantly degrade the quality of the inlet airflow to be inhaled by the aero-engines, thereby, adversely affecting the performance of the aero-engines.

4. Conclusion

An experimental study was conducted to investigate the dynamic ice accretion process over the surfaces of rotating aero-engine spinners and to evaluate the detrimental effects induced by the ice accretion on the quality of the inlet airflow to be inhaled by aero-engines. Three scaled aero-engine spinner-fan models with different kinds of spinner shapes (i.e., elliptical-shaped, conical-shaped, and coniptical-shaped spinners) were manufactured for a comparative study. The experimental study was performed in an icing research tunnel available at Iowa State University (i.e., ISU-IRT) with the test models exposed under two typical icing conditions (i.e., *rime* and *glaze* icing conditions). During the experiments, a high-speed imaging system was used to acquire "phase-locked" ice accretion images to reveal the transient behavior of the dynamic ice accretion process over the surfaces of the rotating spinner models. An image processing procedure was implemented to extract quantitative information from the acquired "phase-locked" ice accretion images to quantify the growth of the ice thickness/mass accumulated over the surfaces of the three compared spinner models. A high-

resolution particle image velocimetry (PIV) system was also used to quantify the trajectories of the super-cooled water droplets as they approach to the spinner models and to examine the detrimental effects induced by the ice accretion over the spinner surfaces on the quality of the inlet airflow to be inhaled by aero-engines.

It was revealed clearly that, upon the impacting of the supercooled water droplets carried in the incoming airflow, ice structures were found to accrete rapidly over the surfaces of the rotating spinner models. Under a typical rime icing condition with relatively colder ambient temperature and lower liquid water content (LWC) level, since the released latent heat of fusion associated with the solidification (i.e., icing process) of the impacted supercooled water droplets could be dissipated rapidly, the impinged water mass was found to turn into ice instantly upon impacting onto the spinner surfaces. While the accreted rime ice layers were found to conform well with the original shapes of the three compared spinners in general, the total amount of the ice mass and coverage of the ice layer accreted over the spinner surfaces were found to be a strong dependent on the shapes of the spinners. While the conical-shaped spinner was found to be most susceptible to rime ice accretion with the largest ice coverage area and greatest accreted ice mass, the coniptical-shaped spinner was found to have the smallest accreted ice mass among the three compared spinner models. The characteristics of dynamic rime icing process revealed from the ice accretion images were correlated with the trajectories of the super-cooled water droplets in the regions near the spinner surfaces to elucidate the underlying physics pertinent to the ice accretion process on the rotating spinner models.

The ice accretion process over the surfaces of the rotating spinner models were found to become much more involved under the *glaze* icing condition with much higher ambient temperature and liquid water level (LWC) in the incoming airflow. Upon the impacting of the supercooled water droplets onto the spinner surfaces, while only a portion of the impacted water mass could not be frozen into ice instantly, unfrozen water would accumulate on the spinner surface, which would flow freely over the icing accreting spinner surfaces. As driven by the aerodynamic shear forces exerted by the incoming airflow, the unfrozen surface water would run back from spinner nose to root. Meanwhile, due to the effects of the centrifugal forces associated with the rotation motion, some of the runback water was found to take off from the spinner surfaces, then frozen into ice subsequently, resulting in the formation of very complicated needle-liked icicle structures over the rotating spinner surfaces. The location and extent of the needle-like icicle structures accreted on the spinner surfaces were found to be strongly dependent on the shapes of the spinners. Among the three compared spinner models, the conical-shaped spinner model was found to have the largest coverage of the needle-liked icicle structures under the glaze icing condition, the needle-liked icicle structures were found to form only at the front portion of the spinner surface for the elliptical-shaped spinner model with most of the rear potion of the spinner surface being totally ice free. The variation characteristics of the centrifugal forces acting on the runback water over the surfaces of the three compared rotating spinner models were used to explain the differences in the experimental observations about the accretion locations and coverage of the needle-liked icicle structures over the spinner surfaces.

Based on the quantitative PIV measurements of the airflow fields around the iced spinner models, it was revealed clearly that, ice structures accreted over the spinner surfaces would cause obvious reductions to the airflow speed near the spinner surfaces and even induce large-scale flow separations in the regions behind complicated glaze ice structures accreted over the spinner surfaces. It indicated that the ice formation/accretion on the aero-engine inlet components, such as on the surfaces of the rotating spinner and fan blades, could significantly degrade the quality of the inlet airflow to be inhaled by the aero-engines. Among the three compared spinner models, the detrimental effects induced by the ice accretion were found to be the most severe around the elliptical-shaped spinner model (i.e., greater flow separation regions over the spinner surface), which is believed to be caused by the much earlier formation of complex needle-liked icicles near the nose of the elliptical-shaped spinner model.

Declaration of Competing Interest

The authors declared that there is no conflict of interest.

Acknowledgments

The authors want to thank Dr. Rye Waldman, Miss. Linyue Gao, Mr. James Benson and Mr. Andrew Jordan of Iowa State University for their help in operating ISU Icing Research Tunnel (ISU-IRT) Facility. The research work is partially supported by Iowa Space Grant Consortium (ISGC) Base Program for Aircraft Icing Studies. The support of National Science Foundation (NSF) under award numbers of CBET-1916380 and CMMI-1824840 is also gratefully acknowledged.

References

[1] A. Linke-Diesinger, Systems of Commercial Turbofan Engines: An Introduction to Systems Functions, Springer, 2008.
[2] C.S. Bidwell, Particle trajectory and icing analysis of the E 3 turbofan engine using LEWICE3D version 3, pp. AIAA 2012-3037, 4th AIAA Atmos. Sp. Environ. Conf. 25–28 June 2012, New Orleans, Louisiana, 2012, https://doi.org/10.4271/2011-38-0048.
[3] J. Zhu, W. Dong, M. Zheng, G. Lei, Q. Zhao, Numerical investigation of heat and mass transfer on an anti-icing inlet cone, J. Propuls. Power. 32 (2016) 789–797, https://doi.org/10.2514/1.B35875.
[4] J. Wang, Y.P. Hu, H.H. Ji, N.L. Chen, G.Z. Cao, Experiment of ice accretion and shedding on rotating spinner, J. Aerosp. Power 29 (2014) 1352–1357, https://doi.org/10.13224/j.cnki.jasp.2014.06.013.
[5] Y.P. Hu, H.H. Ji, J. Wang, N.L. Chen, G.Z. Cao, H. Tong, et al., Experiment on effect of cone angle on ice accretion of rotating spinner, J. Aerosp. Power 29 (2014) 495–503, https://doi.org/10.13224/j.cnki.jasp.2014.03.003.
[6] L. Li, H. Hu, An experimental study of dynamic ice accretion process on aero-engine spinners, 55th AIAA Aerosp. Sci. Meet., Grapevine, Texas, American Institute of Aeronautics and Astronautics, 2017, , https://doi.org/10.2514/6.2017-0551.
[7] U.W. Ganz, P.D. Joppa, T.J. Patten, D.F. Scharpf, Boeing 18-inch fan gig broadband noise test, 1998.
[8] U.S. Government Publishing Office, CFR Title 14 FAA Part 25, 2014.
[9] U.S. Government Publishing Office, CFR Title 14 FAA Part 33, 2014.
[10] Y. Bin, Z. Yanpei, Icing certification of civil aircraft engines, Proc. Eng. 17 (2011) 603–615, https://doi.org/10.1016/j.proeng.2011.10.076.
[11] R.K. Jeck, Icing Design Envelopes (14 CFR Parts 25 and 29, Appendix C) Converted to a Distance-Based Format, Fed. Aviat. Adm. Tech. Cent. Atl. CITY NJ, 2002, pp. 55. http://oai.dtic.mil/oai/oai?verb=getRecord&metadataPrefix=html&identifier=ADA401921 (accessed September 8, 2016).
[12] M.K. Politovich, Predicting glaze or rime ice growth on airfoils, J. Aircr. 37 (n.d.). https://doi.org/10.2514/2.2570.
[13] M. Papadakis, A. Rachman, S. Wong, H. Yeong, C.S. Bidwell, Water Droplet Impingement on Simulated Glaze , Mixed, and Rime Ice Accretions, Nasa/Tm-2007-213961, 2007.
[14] Y. Liu, L.J. Bond, H. Hu, Ultrasonic-attenuation-based technique for ice characterization pertinent to aircraft icing phenomena, AIAA J. (2017) 1–8, https://doi.org/10.2514/1.J055500.
[15] M. Zhang, L. Zhang, Z. Liu, Preliminary research on rotating icing test scaling law, Res. J. Appl. Sci. Eng. Technol. 8 (2014) 803–810, https://doi.org/10.19026/rjaset.8.1037.
[16] EASA, EASA Type-Certificate Data Sheet CFM 56-2 & CFM 56-3, 2008.
[17] W. Tian, A. Ozbay, H. Hu, Effects of incoming surface wind conditions on the wake characteristics and dynamic wind loads acting on a wind turbine model, Phys. Fluids 26 (2014) 125108, https://doi.org/10.1063/1.4904375.
[18] Y. Liu, L. Li, Z. Ning, H. Hu, An experimental study on the transient ice accretion process over a rotating UAV propeller, 55th AIAA Aerosp. Sci. Meet. Grapevine, Texas, January 9–13, 2017, (2017).
[19] R.M. Waldman, H. Hu, High-speed imaging to quantify transient ice accretion process over an airfoil, J. Aircr. 53 (2016) 369–377, https://doi.org/10.2514/1.C033367.
[20] M. Vargas, H. Broughton, J.J. Sims, B. Bleeze, V. Gaines, Local and total density measurements in ice shapes, J. Aircr. 44 (2007) 780–789, https://doi.org/10.2514/1.23326.
[21] Y. Liu, H. Hu, An experimental investigation on the unsteady heat transfer process over an ice accreting airfoil surface, Int. J. Heat Mass Transf. 122 (2018) 707–718, https://doi.org/10.1016/j.ijheatmasstransfer.2018.02.023.
[22] J.J. Lacey, Turbine engine icing and ice detection, p. V001T01A006, ASME 1972 Int. Gas Turbine Fluids Eng. Conf. Prod. Show, 1972, https://doi.org/10.1115/72-GT-6.
[23] S.K. Thomas, R.P. Cassoni, C.D. MacArthur, Aircraft anti-icing and de-icing techniques and modeling, J. Aircr. 33 (1996) 841–854, https://doi.org/10.2514/3.47027.